A Study of the Ballistic Limit of AA2024-T351 Sheets Impacted by Spherical and Cubical Compact Projectiles

Tom DE VUYST[1)], Rade VIGNJEVIC[2)],
Adrian AZORIN ALBERO[3)], Kevin HUGHES[1)],
James C. CAMPBELL[1)], Nenad DJORDJEVIC[1)]

[1)] *Structural Integrity*
Brunel University London
Granta Park, NSIRC, Great Abington, Cambridgshire CB21 6AL
e-mail: tom.devuyst@brunel.ac.uk

[2)] *Structural Integrity*
Brunel University London
Kingston Lane, Uxbridge, Middlesex UB8 3PH
e-mail: v.rade@brunel.ac.uk

[3)] *Applied Mechanics*
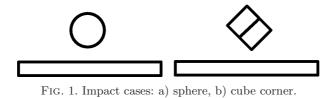*Cranfield University*
Cranfield, Bedfordshire MK43 0AL, UK

This paper presents the results of an investigation of the ballistic limits and failure modes of AA2024-T351 sheets impacted by spherical and cubical projectiles. The investigation included a series of impact experiments and numerical simulations. The lowest ballistic limit (225 m/s) was observed for the spherical projectile. In the cube impacts the ballistic limit was 254 m/s. With the aid of the finite element models it was possible to develop a better understanding of the test results and explain that the observed differences in the impact responses are due to the combination of the localised deformation near the projectile impact point and the resulting global, dishing, deformation.

Key words: ballistic impact, compact projectiles, cube projectiles, failure mode.

1. INTRODUCTION

A significant proportion of the literature on ballistic limit studies is focused on cylindrical projectiles with ogive, flat, conical, and hemispherical nose shapes. For example GUPTA *et al.* studied the ballistic performance of thin AA1100-plates [6, 7, 9] cylindrical projectiles with different nose shapes. In [6] and [7]

AA1100-H12 targets were considered. In [6] this material was used in a study of the ballistic limit of plates of thickness 0.5, 0.71, 1.0, and 1.5 mm thick subjected to impacts with flat, ogive, and hemispherical nosed cylindrical projectiles, and extended to thicknesses of 2.0, 2.5, and 3.0 mm in [7]. These authors also studied the effect of target size in [9]. Experiments were performed where the ratio of the 1 mm thick AA1100-H12 target diameter to projectile diameter was varied from 3.6 to 15, in the simulations a range of 3.6 to 40 was considered.

In [17] SENTHIL and IQBAL studied 1 mm thick monolithic and double-layered plates of 2 stacked 0.5 mm thick sheets made of AA1100-H12 aluminium. In this study the effect of the target thickness to projectile diameter ratio was investigated. The size of the projectile was varied by varying its shank diameter as 15, 19, and 24 mm. It was concluded that the ballistic resistance increased with increasing projectile diameter, and that the monolithic target offered the highest resistance. RODRÍGUEZ-MILLÁN *et al.* considered the impact of flat, conical, and spherical nosed cylinders of diameter 13 mm on 4 mm AA 5754-H111 and AA 6082-T6 plates in [15]. It was observed that the lowest ballistic limit occured for flat nosed projectiles. JANKOWIAK *et al.* [10] performed a numerical study of 2 mm and 4 mm monolithic and layered sheets impacted by conical, hemispherical, and flat nosed cylindrical projectiles. In [14] RUSINEK *et al.* studied the effect of projectile diameter of a conical nosed projectile impacting a Weldox 460 E steel 12 mm thick plate. The ballistic limit increased linearly with projectile diameter. In [1] this was extended by a numerical study of 20 mm diameter blunt, conical, and hemispherical nosed projectiles. The authors concluded that the blunt nosed projectile has the lowest ballistic limit. In [4] BØRVIK *et al.* studied the impact of blunt and ogival 20 mm diameter steel cylinders on AA7075-T651 sheets of thickness 20 mm. The target failure mode is brittle, with fragmentation and delamination failures observed. Regarding compact projectiles (i.e. projectiles with aspect ratio close to one), ERICE [5] considers the impact of 5.55 mm diameter steel spherical projectiles on 1.6 mm thick Inconel 718 plates and JORDAN [11] studies a range of compact fragments, i.e. L/D ratio in the range 0.9–1.3 on glass fibre reinforced plastic (GFRP) sheets with thicknesses of 4, 9, 14 mm. The objective of the work presented in this paper was to investigate the ballistic limit and failure mode for the case of spherical and cubical projectiles. In order to achieve this, a number of ballistic impact experiments and finite element analyses with spherical and cubical projectiles were performed. The cube impact tests were performed such that the cube impacted the target with a corner as shown in Fig. 1. The observed differences in ballistic limit are explained in terms of differences in failure mode. Furthermore the observations are complemented by numerical simulations which allow their more detailed interpretation.

Fig. 1. Impact cases: a) sphere, b) cube corner.

2. Experiments

As mentioned above, in order to evaluate the effect of projectile orientation on ballistic limit, a series of impact tests were performed on 3.175 mm thick AA2024-T351 sheets. The target plates were manufactured from 3.175 mm AA2024-T351 and were clamped at two opposite edges, leaving the other two edges free. The unclamped area of the targets was 120×120 mm. The experiments were performed with a single stage gas gun using high pressure nitrogen to accelerate the projectiles. The barrel used had a length of 2 m and inner diameter of 31 mm. At maximum pressure this allowed projectiles to be accelerated to velocities of around 325 m/s.

The experimental setup is shown in Fig. 2. The velocity of the projectile was measured using an optical velocity measurement system consisting of two light beams. The time interval between the projectile interrupting the two light beams allowed for the velocity of the projectile to be calculated. The projectiles were placed in a sabot for launch, and in order to ensure the corner impact the target was moved as close as possible to the sabot stripper (about 50 mm). The proper alignment was verified with an Olympus i-SPEED 3 high speed camera recording at 30 000 fps. The high speed image (Fig. 3a) shows the location of the target and the cube travelling towards the target with the corner pointing
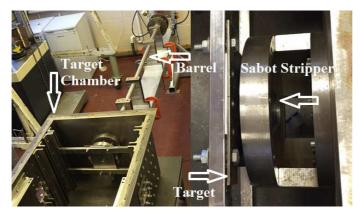

Fig. 2. Experimental setup: overview.

forward. A further verification of the correct impact conditions was possible by the observation of a small plug (4 mm side) which clearly shows the imprint of the corner, see Fig. 3b. This plug is also visible on the high speed image in Fig. 6c.
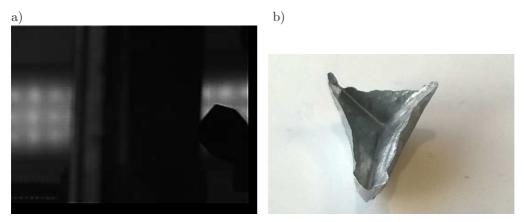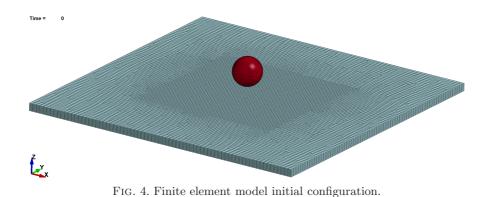
a)

b)

FIG. 3. a) High speed image (projectile travels right to left) showing cube before impact and b) triangular plug formed in cube impact showing cube corner imprint.

3. FINITE ELEMENT MODELLING

An LS-DYNA [13] finite element model was constructed using hypermesh [8] to gain a better insight in the perforation mechanism for both types of projectiles. Projectile and target were modelled with solid elements. Seven elements were defined through the thickness of the plate resulting in an element size of 0.45 mm in the through thickness direction. In the in-plane directions an element size of 0.8 mm was used in the impact location, coarsening to 1.6 mm in the rest of the target, see Fig. 4. This ensured that the aspect ratio of the

FIG. 4. Finite element model initial configuration.

elements in the impact area was kept below a 1:2 ratio. Reducing the element size by a factor of two to 0.4 mm resulted in a change of ballistic limit of less than 5%, virtually identical residual velocities above the ballistic limit and very similar failure patterns. Hence the 0.8 mm element size mesh was used in the remainder of the paper. The element size used in the projectile was 0.7 mm, and the eroding single surface contact algorithm available in LS-DYNA was used to model the interaction between target and projectile. The default penalty coefficients were used and a coefficient of friction of 0.5 was defined. In order to prevent non-physical interpenetration the segment based contact was used with checks on surface and edge-to-edge penetrations activated [13].

3.1. Constitutive models

The projectile behaviour was modelled using an elastic perfectly-plastic material model and the material properties used are listed in Table 1.

Table 1. Steel cube material model parameters [3].

Material	Density [kg/m^3]	Young's modulus [GPa]	Poisson's ratio [–]	Yield stress [MPa]
Steel	7740	206.8	0.33	470

Regarding the model used for the target, the anisotropic plasticity model proposed by BARLAT et al. in [2] was used. This model was chosen because the work by SEIDT et al. [17] showed that the accuracy of predicting ballistic limits of AA2024 sheets can be improved by taking into account anisotropy using the Barlat constitutive model as opposed to an isotropic yield criterion. This six parameter model uses an associative flow rule:

$$(3.1) \qquad \dot{\epsilon}_{ij} = \lambda \frac{\partial f}{\partial \sigma_{ij}}$$

and yield function:

$$(3.2) \qquad f = \overline{\sigma} - \sigma_{flow}\left(\overline{\epsilon}^p\right)$$

and $\overline{\sigma}$ is the equivalent stress [13] which is defined as:

$$(3.3) \qquad 2\overline{\sigma}^m = |S_1 - S_2|^m + |S_1 - S_2|^m + |S_1 - S_2|^m,$$

where S_1, S_2, and S_3 are the principal values of the symmetric matrix S with components

$$S_{xx} = \left[c \left(\sigma_{xx} - \sigma_{yy} \right) - b \left(\sigma_{zz} - \sigma_{xx} \right) \right] / 3,$$
$$S_{yy} = \left[a \left(\sigma_{yy} - \sigma_{zz} \right) - c \left(\sigma_{xx} - \sigma_{yy} \right) \right] / 3,$$
$$S_{zz} = \left[b \left(\sigma_{zz} - \sigma_{xx} \right) - a \left(\sigma_{yy} - \sigma_{zz} \right) \right] / 3,$$
$$S_{yz} = f \sigma_{yz}, \quad S_{zx} = g \sigma_{zx}, \quad S_{xy} = h \sigma_{xy}$$

and a, b, c, f, g, h are the six parameters required to describe the shape of the yield surface. The implementation in LS-DYNA of this model is completed by defining the flow stress as a function of effective plastic strain, $\sigma_{flow} \left(\overline{\epsilon}^p \right)$. Apart from these parameters the elastic part of the model is defined by Young's modulus E and Poisson's ratio ν. The values of the model parameters were based on published data by SEIDT *et al.* [17] and BARLAT [2] for the aluminium sheet. The Young's modulus (73.084 GPa), density (2770 kg/m^3), and the yield function parameters a, b, c, f, g, and h accounting for anisotropic response were the parameters BARLAT *et at.* [3] identified for the case of an AA2024-T3 sheet (see Table 2). The flow stress versus effective plastic strain curve was defined using the data provided in SEIDT *et al.* [17].

Table 2. Sets of parameters used for Barlat's six-component anisotropic plasticity model [2].

Type	m	a	b	c	f	g	h
Anisotropic	8	1.378	1.044	0.955	1.0	1.0	1.210

In this material model failure can be modelled through a maximum principal strain at failure element erosion criterion available in LS-DYNA. A value of 0.165 was set for the maximum principal strain at failure. This value was determined by comparing the ballistic limit predictions using this model with a Johnson-Cook model which includes a temperature, strain rate, and stress axiality dependent failure criterion. The comparison was made using sphere impact test data on AA2024-T3 published by KELLEY and JOHNSON [12].

4. RESULTS AND DISCUSSION

4.1. Results overview

The test results (impact and residual velocities) are summarised in Table 3 and plot in Fig. 5. This plot also shows the result of fitting the parameters a

Table 3. Summary of impact and residual velocities for experiments,
FE simulations and Recht-Ipson equation.

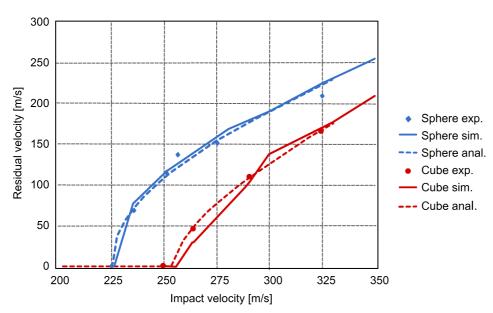| Projectile	v_i [m/s]	v_r (exp) [m/s]	v_r (sim) [m/s]	v_r (analyt) [m/s]
Sphere	225	0	0	0
Sphere	235	69	79	71
Sphere	251	116	118	111
Sphere	256	137	128	122
Sphere	275	152	160	155
Sphere	325	210	225	224
Cube	249	0	0	0
Cube	263	47	30	48
Cube	290	111	104	110
Cube	324	167	169	168

FIG. 5. Ballistic limit curve, Recht-Ipson equation fit and simulation results.

and p of a RECHT-IPSON [4] equation to the experimental data (parameters summarised in Table 4).

$$(4.1) \qquad v_r = a \left(v_i^p - v_{bl}^p \right)^{1/p},$$

where

(4.2)
$$a = \frac{m_{\mathrm{projectile}}}{m_{\mathrm{projectile}} + m_{\mathrm{plug}}}.$$

Table 4. Summary of parameters for the Recht-Ipson equation.

Type	Ballistic limit [m/s]	p	a
Sphere	225	2.16	0.91
Cube	254	1.97	1.00

The ballistic limit for sphere and cube impacts is 225 and 254 m/s respectively. In order to explain this 13% difference in ballistic limit the effect of projectile projected area and failure mode will be discussed in more detail in the next sections. The residual velocities obtained by the finite element modelling are also summarised in Table 3, and plot in Fig. 5. The finite element results correlate well with the experimental data for both cases. The RMS error between experimental and simulation results is 3.7 m/s for the sphere impact and 4.7 m/s for the cube impact. The ballistic limit predicted by the simulation is 227 m/s for the sphere impact and 259 m/s for the cube impact. The errors in the ballistic limit prediction are 1% and 2% for the sphere and cube impact respectively.

4.2. *Penetration mechanism*

Sphere. The penetration mechanism for the spherical projectile impacts on the target was a combination of plugging, radial fractures (petalling), and dishing. According to [19] the dishing deformation was expected since the target thickness was approximately three times smaller than the projectile diameter. The plug formation was clearly visible in the high speed pictures, see Fig. 6a. In all high speed camera images the direction of travel of the projectile is from right to left. The failure mode did not change over the velocity range tested. The diameters of the holes, between 11.2 mm at 235 m/s to 11.4 mm at 325 m/s, were smaller than the projectile diameter (11.9 mm). Hence, penetration occurred after the plate deformed in bending combined with radial cracking. This was then followed by elastic unloading which brought the hole to its final diameter smaller than the diameter of the projectile.

Cube. In the case of the corner impact the failure mechanism was different than for the sphere impact. First a small triangular fragment was created
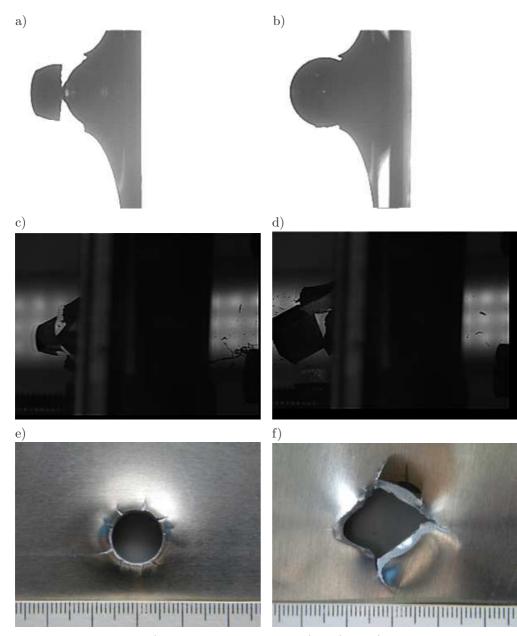
a)

b)

c)

d)

e)

f)

Fig. 6. High speed image (projectile travels right to left) of: a) and b) sphere showing plugging, and c) and d) corner impact showing fragment ejection. Deformed state for: e) sphere, f) corner impact.

through tensile failure around the corner contact point, as can be seen in Fig. 6c. From this initial perforation three cracks (corresponding to the edges which intersect at the impact corner) then propagated. This resulted in the formation

of three petals. As the projectile advances these petals bend and become larger (see Fig. 6d), in some cases breaking off as shown in Fig. 6f.

4.3. Localised deformation and dishing

A comparison of measured and simulated plate deflections in the transverse/longitudinal direction (clamping direction) is shown in Fig. 7.
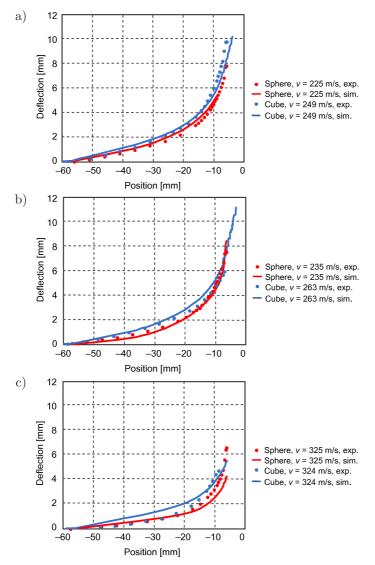

FIG. 7. Global deformations for impact velocity a) below ballistic limit, b) above ballistic limit, and c) at 325 m/s.

Sphere. The number of radial cracks was 9 cracks for the 235 m/s impact and 10 cracks at 325 m/s. The amount of dishing decreased with increase in impact velocity. The maximum deflection for impact of 235 m/s was 8.0 mm and for impact velocity of 325 m/s maximum deflection was 6.6 mm, the simulations predict the same trend with deflections of 8.4 and 4.2 mm respectively. At the same time the plug velocity increases in an almost linear fashion from 177 m/s to 293 m/s for impact speeds of 225 and 325 m/s respectively. The diameter of the hole for the sphere impact does not vary over the range of impact velocities tested and is on average 11.1 mm.

Cube. For this failure mode it was not straightforward to define a good measure for the size of the hole in the plate. Measuring hole in the direction of the clamped edges and the direction perpendicular to it results in hole dimensions of roughly 15 mm, with lower and upper bounds of 10 and 20 mm. The simulations predict similar dimensions of approximately 15 mm. The dishing of the plate, see Fig. 7, is higher than in the sphere impact configuration. The maximum out of plane deflection decreased slightly with increasing impact speed (see Fig. 7). The deflection at 264 m/s is 4.6 mm and at 325 m/s 4.4 mm, the simulations predict similar deflections of 5.1 and 3.9 mm respectively. Due to the shape of the hole, with three petals, it is difficult to define a good measure for the size of the hole. However, the average dimension of the hole measures 15 mm for the cube impact.

4.4. Energy absorption and contact force

Figure 8 shows the projectile kinetic energy loss as a function of impact velocity. The points with hollow markers are associated with impacts below the
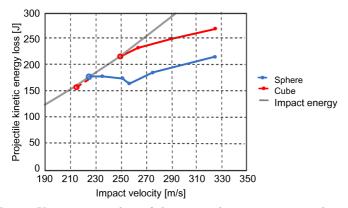

FIG. 8. Kinetic energy loss of the projectile versus impact velocity.

ballistic limit. This figure shows that for the velocity range studied, the energy loss increased with impact velocity for both cases.

In order to explain the difference in ballistic limit one can consider the effect of the different projectile nose area for these four impact configurations similar to the analysis by RUSINEK [14] which shows that the velocity lost by conical nosed projectiles is proportional to the square root of the projectile diameter (or projectile nose area), and in that case curves of velocity lost per unit area as a function of impact speed for different projectile diameters collapse on to one single curve. Figure 9 shows the velocity lost per unit area versus the impact velocity for the impact case considered. It is clear that the curves do not collapse on to one single curve, and that therefore the difference in ballistic limit observed cannot be attributed to solely the difference in projectile nose area. This means that the differences in penetration mechanism between each impact configuration also play a role.
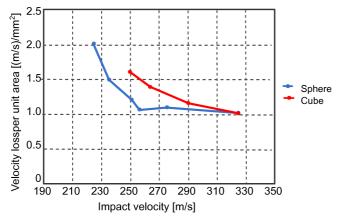

FIG. 9. Velocity loss per unit projectile area versus impact velocity.

Figure 10 shows the evolution of the contact force and the kinetic energy loss of the projectile as a function of time. Since the amount of dishing does not change significantly, the increase in energy absorbed with increasing velocity (see Fig. 8) is due to more energy being absorbed in local deformation. Considering the impact energy absorption it can be seen that the corner impact results in the most gradual, and the sphere impact results in the faster reduction of projectile kinetic energy. This can be explained by the gradual increase of the contact area in the corner case, while for the sphere impact the contact area is established more rapidly and results in a plug being ejected. The contact force time histories for impacts below the ballistic limit are similar in magnitude, shape, and duration, see Fig. 10a. Both curves show an initial peak in contact force followed by a period of roughly 100 μs with a more or less constant contact
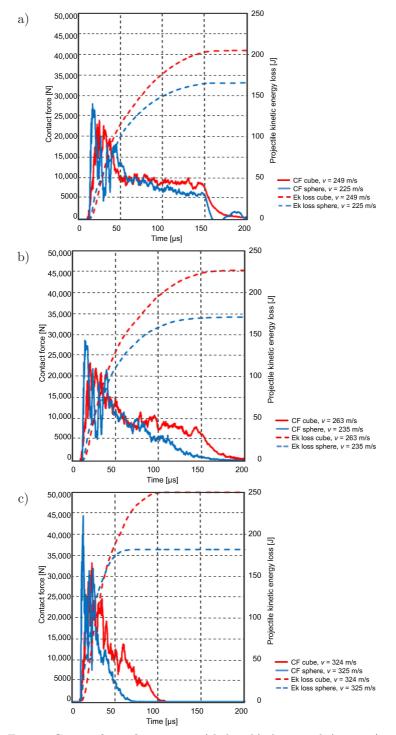
Fig. 10. Contact forces for impacts: a) below, b) above, and c) 325 m/s.

force. The initial rise in contact force is faster for the sphere impact case, and this results in a faster drop in projectile kinetic energy. If one compares the contact force and the projectile kinetic energy loss time histories of the two impact configurations for an impact velocity just above their respective ballistic limits (see Fig. 10b) then one observes a change in shape for the sphere impact configuration. At time about 30 μs after impact the plug is formed and the contact force then gradually drops to zero, while the cube impact still shows a period of constant contact force as the projectile perforates the target. At the highest impact velocity tested (respectively 325 and 324 m/s for the sphere and cube) the contact interaction lasts only 50 μs for the sphere and 100 μs for the cube. The longer interaction time of the cube projectile results in a 40% increase in energy absorbed compared to the sphere impact.

5. Conclusion

In this paper the response of 3.175 mm thick AA2024-T351 sheets to impact by spherical and cubical projectiles was determined through a study of impact experiments and simulations. The results show that for a 3.175 mm thick AA2024-T351 sheet the lowest ballistic limit (225 m/s) was observed for the sphere impact, while the highest ballistic limit was observed for a cube impact with a corner (254 m/s). The difference in ballistic limit between the two projectiles is due to the different way momentum is transferred from the projectile to the target, which results in different failure mechanisms. The cubical projectile impact results in energy absorption through the development of three large petals, while the spherical projectile generates a plug and short radial cracks. The cubical projectile also interacts longer with the target than the sphere which results in a slower reduction of projectile kinetic energy and more energy absorption through dishing. Over the velocity range tested both shapes of projectiles show an increase in absorbed energy by the target with increasing impact speed.

REFERENCES

1. ARIAS A., RODRÍGUEZ-MARTÍNEZ J.A., RUSINEK A., *Numerical simulations of impact behaviour of thin steel plates subjected to cylindrical, conical and hemispherical non-deformable projectiles*, Engineering Fracture Mechanics, **75**(6): 1635–1656, 2008, http://www.sciencedirect.com/science/article/pii/S0013794407002767.

2. BARLAT F., LEGE D.J., BREM J.C., *A six-component yield function for anisotropic materials*, International Journal of Plasticity, **7**: 693–712, 1991, http://www.sciencedirect.com/science/article/pii/074964199190052Z.

3. BUYUK M., LOIKKANEN M., KAN C.S., *A computational and experimental analysis of ballistic impact to sheet metal aircraft structures*, 5th Europe LS-DYNA Users Conference, 2005.

4. BØRVIK T., HOPPERSTAD O.S., PEDERSEN K.O., *Quasi-brittle fracture during structural impact of AA7075-T651 aluminium plates*, International Journal of Impact Engineering, **37**(5): 537–551, 2010, http://www.sciencedirect.com/science/article/pii/S0734743X09001924.

5. ERICE B., PÉREZ-MARTÍN M.J., GÁLVEZ F., *An experimental and numerical study of ductile failure under quasi-static and impact loadings of Inconel 718 nickel-base superalloy*, International Journal of Impact Engineering, **69**: 11–24, 2014, http://www.sciencedirect.com/science/article/pii/S0734743X14000384.

6. GUPTA N.K., IQBAL M.A., SEKHON G.S., *Effect of projectile nose shape, impact velocity and target thickness on the deformation behavior of layered plates*, International Journal of Impact Engineering, **35**(1): 37–60, 2008, http://www.sciencedirect.com/science/article/pii/S0734743X06003186.

7. GUPTA N.K., IQBAL M.A., SEKHON G.S., *Effect of projectile nose shape, impact velocity and target thickness on deformation behavior of aluminum plates*, International Journal of Solids and Structures, **44**(10): 3411–3439, 2007, http://www.sciencedirect.com/science/article/pii/S0020768306004045.

8. Hypermesh, http://www.altairhyperworks.co.uk, accessed online 14/08/2015.

9. IQBAL M.A., TIWARI G., GUPTA P.K., BHARGAVA P., *Ballistic performance and energy absorption characteristics of thin aluminium plates*, International Journal of Impact Engineering, **77**: 1–15, 2015, http://www.sciencedirect.com/science/article/pii/S0734743X1400253X.

10. JANKOWIAK T., RUSINEK A., WOOD P., *A numerical analysis of the dynamic behaviour of sheet steel perforated by a conical projectile under ballistic conditions*, Finite Elements in Analysis and Design, **65**: 39–49, 2013, http://www.sciencedirect.com/science/article/pii/S0168874X12001989.

11. JORDAN J.B., NAITO C.J., *An experimental investigation of the effect of nose shape on fragments penetrating GFRP*, International Journal of Impact Engineering, **63**: 63–71, 2014, http://www.sciencedirect.com/science/article/pii/S0734743X13001577.

12. KELLEY S., JOHNSON G., *Statistical testing of aircraft materials for transport airplane rotor burst fragment shielding*, Report for U.S. Department of Transportation Federal Aviation Administration, Report no. DOT/FAA/AR-06/9, May 2006, http://www.tc.faa.gov/its/worldpac/techrpt/AR06-9.pdf.

13. LS-DYNA Keyword User's Manual, Vol. I–II, Livermore Software Technology Corporation (LSTC), 2013.

14. RUSINEK A., RODRÍGUEZ-MARTÍNEZ J.A., ARIAS A., KLEPACZKO J.R., LÓPEZ-PUENTE J., *Influence of conical projectile diameter on perpendicular impact of thin steel plate*, Engineering Fracture Mechanics, **75**(10): 2946–2967, 2008, http://www.sciencedirect.com/science/article/pii/S0013794408000143.

15. RODRÍGUEZ-MILLÁN M., VAZ-ROMERO A., RUSINEK A., RODRÍGUEZ-MARTÍNEZ J.A., ARIAS A., *Experimental study on the perforation process of 5754-H111 and 6082-T6 aluminium plates subjected to normal impact by conical, hemispherical and blunt projectiles*, Experimental Mechanics, **54**(5): 729–742, 2014, http://link.springer.com/article/10.1007%2Fs11340-013-9829-z#/page-1.

16. TIWARI G., IQBAL M.A., GUPTA P.K., GUPTA N.K., *The ballistic resistance of thin aluminium plates with varying degrees of fixity along the circumference*, International Journal of Impact Engineering, **74**: 46–56, December 2014, http://www.sciencedirect.com/science/article/pii/S0734743X14000220.

17. SEIDT J.D., MICHAEL PEREIRA J., GILAT A., REVILOCK D.M., NANDWANA K., *Ballistic impact of anisotropic 2024 aluminum sheet and plate*, International Journal of Impact Engineering, **62**: 27–34, 2013, http://www.sciencedirect.com/science/article/pii/S0734743X13001152.

18. SENTHIL K., IQBAL M.A., *Effect of projectile diameter on ballistic resistance and failure mechanism of single and layered aluminum plates*, Theoretical and Applied Fracture Mechanics, **66–67**: 53–64, 2013, http://www.sciencedirect.com/science/article/pii/S016784421300089X.

19. WOODWARD R.L., *The interrelation of failure modes observed in the penetration of metallic targets*, International Journal of Impact Engineering, **2**(2): 121–129, 1984, http://www.sciencedirect.com/science/article/pii/0734743X84900010.